Journal of Materials Science & Technology 108 (2022) 186–195

Contents lists available at ScienceDirect

Journal of Materials Science & Technology

journal homepage: www.elsevier.com/locate/jmst

Direct synthesis of Fe-Si-B-C–Cu nanocrystalline alloys with superior soft magnetic properties and ductile by melt-spinning

Xingjie Jia[a,b], Bojun Zhang[a], Wei Zhang[b,*], Yaqiang Dong[a,c,*], Jiawei Li[a,c], Aina He[a,c], Run-Wei Li[a,c]

[a] Zhejiang Province Key Laboratory of Magnetic Materials and Application Technology, CAS Key Laboratory of Magnetic Materials and Devices, Ningbo Institute of Materials Technology & Engineering, Chinese Academy of Sciences, Ningbo 315201, China
[b] Key Laboratory of Solidification Control and Digital Preparation Technology (Liaoning Province), School of Materials Science and Engineering, Dalian University of Technology, Dalian 116024, China
[c] University of Chinese Academy of Sciences, Beijing 100049, China

ARTICLE INFO

Article history:
Received 18 May 2021
Revised 29 July 2021
Accepted 11 August 2021
Available online 28 October 2021

Keywords:
Fe-based nanocrystalline alloys
High saturation magnetic flux density
Direct synthesis
Melt-spinning
Ductile

ABSTRACT

Structure, magnetic properties and ductile of melt-spun $Fe_{83-x}Si_4B_{13-y}C_yCu_x$ (x = 0–1.7; y = 0–8) alloys were investigated. The addition of 1.7 at.% Cu in a $Fe_{83}Si_4B_{13}$ amorphous alloy generates abundant α-Fe crystals by providing nucleation sites, and further C doping promotes the growth of the crystals by suitable turning amorphous-forming ability, hence they increase saturation magnetic flux density (B_s) and slightly worse magnetic softness of the as-spun alloys. The as-spun $Fe_{81.3}Si_4B_7C_6Cu_{1.7}$ alloy possesses a combined structure of a fully amorphous layer in wheel side surface and predominating nanocrystalline structure with gradually enlarged α-Fe crystal, whose average size and volume fraction are determined as about 12 nm and 32%, respectively, therefore superior soft magnetic properties and ductile with a high B_s of 1.74 T, coercivity (H_c) of 32.7 A/m, effective permeability (μ_e, at 1 kHz) of 3200 and high relatively strain at fracture (ε_f) of 3.61% can be achieved directly in this alloy by only using melt-spinning. The annealing at 578 K releases internal stress, promotes the growth of the α-Fe crystals and remains the amorphous layer of the $Fe_{81.3}Si_4B_7C_6Cu_{1.7}$ alloy, then improves the soft magnetic properties and maintains the superior ductile with increasing the B_s and μ_e to 1.80 T and 14,100, respectively, lowering the H_c to 9.4 A/m and slightly reducing the ε_f to 2.39%. The combination of superior soft magnetic properties and ductile and simplified synthesis process entitles the Fe-Si-B-C–Cu nanocrystalline alloys great potentials in high performance electromagnetic applications.

1. Introduction

Soft magnetic materials have been widely applied as magnetic cores in inductors, sensors, motors and transformers. Silicon steels are the most major soft magnetic materials in practical use because of their high saturation magnetic flux density (B_s) of around 2.0 T and good manufacturability, while they wastes a large amount of power resources because of their relatively high core loss [1, 2]. Nowadays, the electromagnetic devices are developing towards the directions of miniaturization and energy conservation, thus much effort has been devoted in improving materials with high B_s and excellent magnetic softness [2–7]. Among developed soft magnetic materials, Fe-based nanocrystalline alloys have drawn considerable attention due to their high permeability, low coercivity (H_c) and core loss in high frequency. The Fe-Si-B-Nb-Cu nanocrystalline alloys (FINEMET), known as the first nanocrystalline soft magnetic materials developed by Yoshizawa et al. in 1988, have been widely used in magnetic cores because of their excellent soft magnetic properties [7]. The Fe-B(-Cu), Fe-Si-B-Cu and Fe-Si-B-P-Cu nanocrystalline alloys developed in recent years possess high B_s of 1.8–2.0 T, low H_c and core loss, which entitles them great potentials in high-performance electromagnetic applications [6, 8-12]. The excellent magnetic softness of the Fe-based nanocrystalline alloys originates from their unique composite structure composed of nano-sized α-Fe crystals dispersing uniformly in residual amorphous phase [1, 7, 13, 14]. The synthesis processes of such nanocrystalline structure always contain the preparation of amorphous precursors by melt-spinning and subsequent formation of α-Fe phase by annealing. For the FINEMET alloys, the amorphous precursors need to be annealed at 843–853 K for 60 min to achieve the optimal nanostructure [7]. For the latterly developed Fe-Si-B-Cu, Fe-(Si, B, P)-Cu and Fe-B(-Cu) al-

* Corresponding authors.
E-mail addresses: wzhang@dlut.edu.cn (W. Zhang), dongyq@nimte.ac.cn (Y. Dong).

https://doi.org/10.1016/j.jmst.2021.08.055
1005-0302/

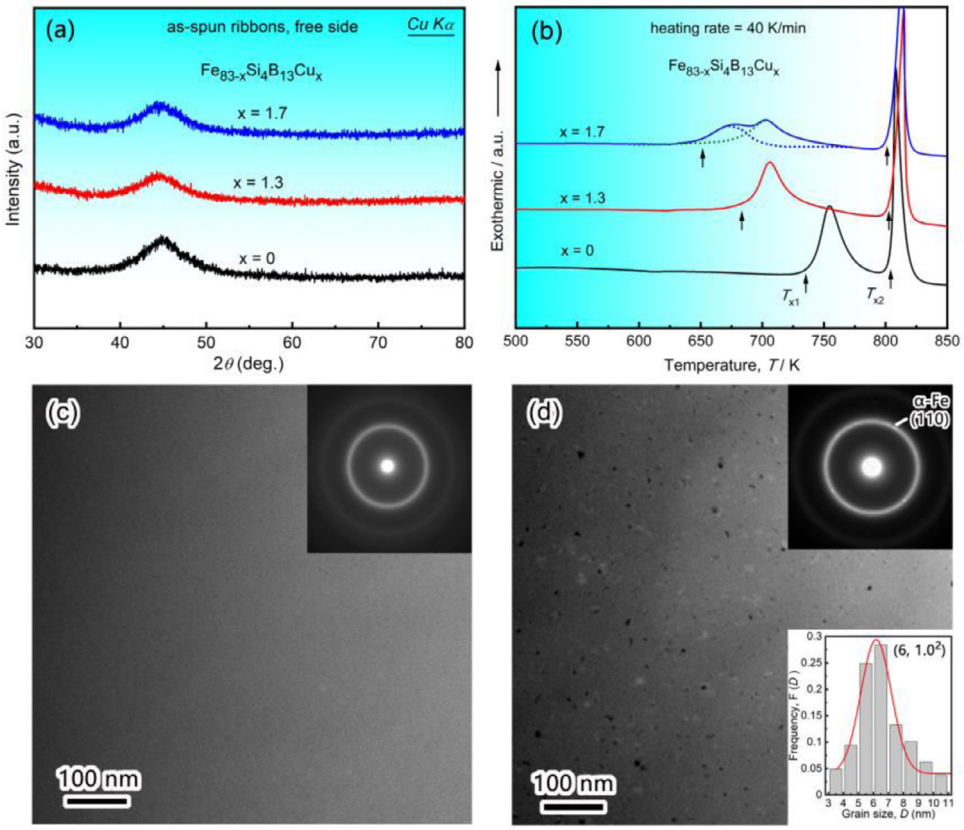

Fig. 1. XRD patterns of free side (a), DSC curves (b), bright-field TEM images of central part of the ribbons, corresponding SAED patterns and gain size distributions (c, d) for as-spun $Fe_{83-x}Si_4B_{13}Cu_x$ alloys. (c) $x = 0$; (d) $x = 1.7$.

loy systems, the melt-spun precursors need to be annealed under high heating rates (H_r) of about 400–9000 K/min to obtain fine α-Fe crystals [10, 11, 15]. The high annealing temperatures (T_a) and H_r consume a large amount of power resources and increase the technical difficulty of annealing processes. In addition, Fe-based nanocrystalline alloys also have a poor ductile after annealing, which hinders the assembling process and reduces the resistance to acoustic vibrations in service [16, 17]. Therefore, eliminating the high T_a and H_r and improve the ductile will be of great significance in synthesis and application of Fe-based nanocrystalline soft magnetic alloys.

Integrating the formation of α-Fe phase into the melt-spinning could greatly simplify the synthesis processes of Fe-based nanocrystalline alloys. Actually, the precipitation of α-Fe phase during melt-spinning is a common phenomenon for high Fe content Fe-(Si, B, P, C)-Cu alloys, while it only happens on the free surface, which always deteriorate the magnetic softness of corresponding nanocrystalline alloys and has no positive effect on improving ductile [18–21]. In addition, Wang et al. synthesized Fe-Ni-Si-B nanocrystalline alloys with good ductility just using the melt-spinning method, but these alloys have relatively large average α-Fe crystals sizes (D) of 28–44 nm and low B_s of 1.54–1.57 T [22]. Therefore, the fabrication of Fe-based nanocrystalline alloys with fine α-Fe crystals, excellent soft magnetic properties and ductile only using melt-spinning method is still a great challenge.

Overviewing the nanocrystallization processes of the well-known Fe-Si-B-Nb-Cu and Fe-Si-B-P-Cu nanocrystalline alloys, the formation of fine α-Fe crystals needs the nucleation of α-Fe phase with a high number density (N_d) and their sufficient growth [15, 23]. The nucleation of α-Fe phase is usually triggered by Cu-enriched clusters [23, 24], whose formation opportunity increases with the rise of Cu content [23], hence it's deduced that a high Cu content will produce a large number of Cu-enriched clusters and then stimulate the precipitation of α-Fe nuclei with a high N_d during melt-spinning. On the other hand, the melt-spun structure of Fe-based alloys is greatly affected by their amorphous-forming ability (AFA), and an appropriate AFA may facilitate the growth of α-Fe phase and prevent the precipitation of non-soft magnetic Fe-B phases. Metalloid elements play an important role in formation of Fe-based amorphous alloys [24–31]. Doping carbon is an effective way in turning AFA of Fe-based alloys without deteriorating their B_s [26–29], therefore it may adjust the growth of α-Fe nuclei of Fe-based alloys during melt-spinning. The ductile of Fe-based nanocrystalline alloys depends on their microstructure. Refining α-Fe crystals and controlling volume fraction of α-Fe phase (V_{cry}) could reduce the formation opportunity of cracks, blunt them and decelerate their growth during bending, which provides theoretical basics to improving ductile of Fe-based nanocrystalline alloys [17, 32].

In present work, with the aim of direct synthesizing Fe-based nanocrystalline alloys with fine α-Fe crystals, superior soft magnetic properties and ductile by melt-spinning, we studied the effects of Cu and C content on structure and properties of melt-spun $Fe_{83-x}Si_4B_{13-y}C_yCu_x$ alloys. It's found that the addition of 1.7 at.% Cu in a $Fe_{83}Si_4B_{13}$ amorphous alloy generates a large quantity of α-Fe crystals in the as-spun alloy and following carbon doping promotes the growth of the crystals, and then a $Fe_{81.3}Si_4B_7C_6Cu_{1.7}$ nanocrystalline alloy with a small D of 12 nm, high B_s of 1.74 T and excellent magnetic softness can be obtained by only using melt-spinning. Besides, due to the combined structure of a fully amorphous layer in wheel side surface and predominating nanocrystalline structure with gradually increasing α-Fe crystal size from

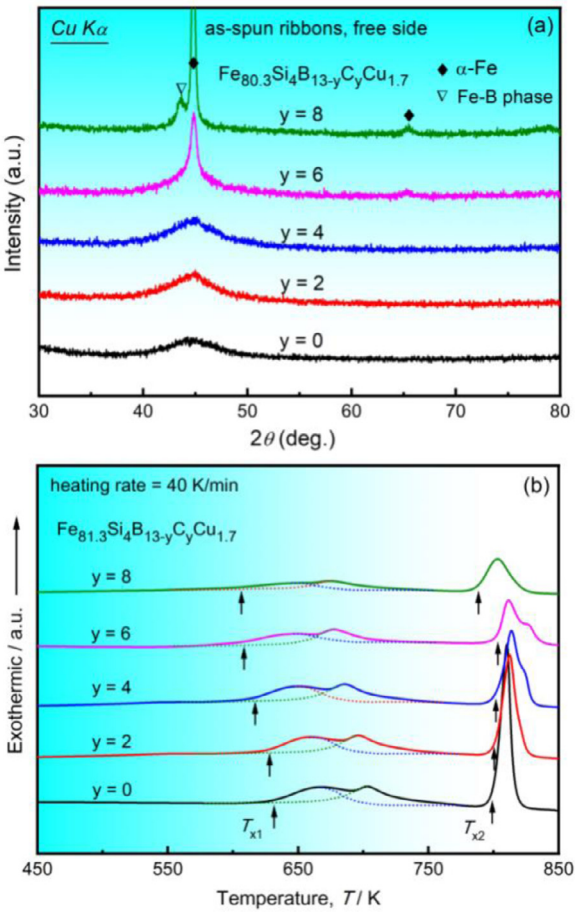

Fig. 2. XRD patterns of free side and DSC curves for as-spun $Fe_{81.3}Si_4B_{13-y}C_yCu_{1.7}$ alloys.

wheel to free side, which endows the as-spun $Fe_{81.3}Si_4B_7C_6Cu_{1.7}$ nanocrystalline alloy a superior ductile as compared with traditional Fe-based nanocrystalline alloys. Furthermore, the effects of annealing on the evolutions of structure and properties of the $Fe_{81.3}Si_4B_7C_6Cu_{1.7}$ nanocrystalline alloy were also studied systematically.

2. Experimental procedure

Alloy ingots with nominal compositions of $Fe_{83-x}Si_4B_{13-y}C_yCu_x$ (x = 0–1.7; y = 0–8) were prepared by alloying Fe (99.95 mass%), Si (99.999 mass%), B (99.9 mass%), Cu (99.99 mass%) and FeC alloys (99.99 mass%) in an arc melting furnace under an argon atmosphere. The mass losses were less than 0.2 mass%. Ribbon samples with a width of about 1.5 mm and thicknesses of about 20 μm were prepared by singer roller melt-spinning under an argon atmosphere. The as-spun ribbons were isothermally annealed in a muffle furnace 60 min under a H_r of about 20 K min^{-1} followed by water quenching. The structure of the samples was examined by X-ray diffraction with CuK_α radiation and transmission electron microscopy (TEM). The various parts of the ribbons in TEM experiments were achieved by controlling the ion-milling time of free and wheel sides. For the TEM samples of middle part, wheel and free side surfaces of the ribbons, the millings performed from both sides, single free side and single wheel side, respectively, with a voltage and angle of 4.5 keV and 8°, respectively, for 60 min, and then decreased the voltage and angle to 4.0 keV and 6°, respectively, until small holes appeared and the milled times were about 90 min. Eventually, modified the holes by milling the samples from both sides with a voltage and angle of 3.0 keV and 4°, respectively, for 2 min. For the TEM samples of shallow surface in wheel side, the millings performed from both sides with a voltage and angle of 4.5 keV and 8°, respectively, for 15 min, then adjusted both ion guns to single free side of ribbons and milled the samples for 45 min, and then decreased the voltage and angle to 4.0 keV and 6°, respectively, until small holes appeared and the milled times were about 90 min. Eventually, modified the holes by milling the samples from both sides with a voltage and angle of 3.0 keV and 4°, respectively, for 2 min. The D was estimated by using Scherrer formula from the full width at half maximum of the (110) peak in XRD patterns or fitting the size distribution of the crystals in a selected TEM image. The N_d of the crystals was estimated by $N_d = N/(A \times D)$, where N is quantity of the crystals and A is the area of the TEM image [33]. The V_{cry} was estimated by using $V_{cry} = N_d \pi D^3/6$ [32, 34-36]. The B_s was measured by a vibrating sample magnetometer under a maximum applied field of 800 kA m^{-1}. The density used in calculations of B_s was measured by the Archimedean method using diethyl terephthalate. The H_c was measured using straight ribbons with a length of 60 mm by a dc B-H loop tracer. The effective permeability (μ_e) was measured by an impedance analyzer under an applied field of 1 A/m and frequency of 1 kHz. The magnetic domains were investigated by a magneto-optical Kerr microscopy on free side surface of the ribbons. The ductile was measured by using a bending test method with the free side of the ribbons under tensile stress. The relatively strain at fracture (ε_f) was calculated using the expression: $\varepsilon_f = t / (d - t)$, where t is thickness of the ribbon and d is board spacing when the ribbons have just broken [32]. The samples were measured 10 times and the ε_f values were obtained by averaging the data after taking out the maximum and minimum. The morphology of the samples after bending tests was examined by a scanning electron microscopy.

3. Results and discussion

Fig. 1 exhibits XRD patterns of free side, DSC curves, bright-field TEM images of the central part of the ribbons, corresponding selected area electron diffraction (SAED) patterns and gain size distributions for as-spun $Fe_{83-x}Si_4B_{13}Cu_x$ alloys. The red lines in gain size distributions show the normal distribution, and the numbers are the desired value and standard deviation, respectively. The dash lines in DSC curve of x = 1.7 alloy show the Gaussian fittings of the exothermic peaks. The XRD patterns of the alloys contain of only broad peaks (see Fig. 1(a)). The TEM image of the x = 0 alloy has no distinct contrast and the corresponding SAED pattern shows a full halo ring without any detectable diffraction spots (see Fig. 1(c)), suggesting its fully amorphous structure. While the x = 1.7 alloy shows a composite structure of α-Fe crystals (identified by the SAED patterns) with a D of 6 nm and N_d of 2×10^{23} m^{-3} dispersing in the amorphous matrix (see Fig. 1(d)). The XRD and TEM results indicate that the addition of 1.7 at.% Cu in a $Fe_{83}Si_4B_{13}$ alloy could generate a large number of α-Fe crystals, but its V_{cry} is estimated to be about 5%, which is much smaller than that of conventional Fe-based nanocrystalline alloys [15, 32, 37]. The absence of Bragg peaks for α-Fe phase in the XRD patterns can be attributed to the small V_{cry} of α-Fe phase [34, 38]. DSC curves of the x = 0 and 1.3 alloys have two exothermic peaks that associated with the precipitations of α-Fe phase (the onset temperature is marked as T_{x1}) and non-soft magnetic Fe-B phases (the onset temperature is marked as T_{x2}), respectively (see Fig. 1(b)). The rise of Cu content decreases T_{x1} gradually, suggesting that Cu could promote the precipitation of α-Fe phase. It should be noticed that DSC curve of the x = 1.7 alloy contains two overlapped exothermic peaks for the precipitations of α-Fe phase (see Fig. 1(b)), which have been clarified as the growth of α-Fe crystals in as-spun state

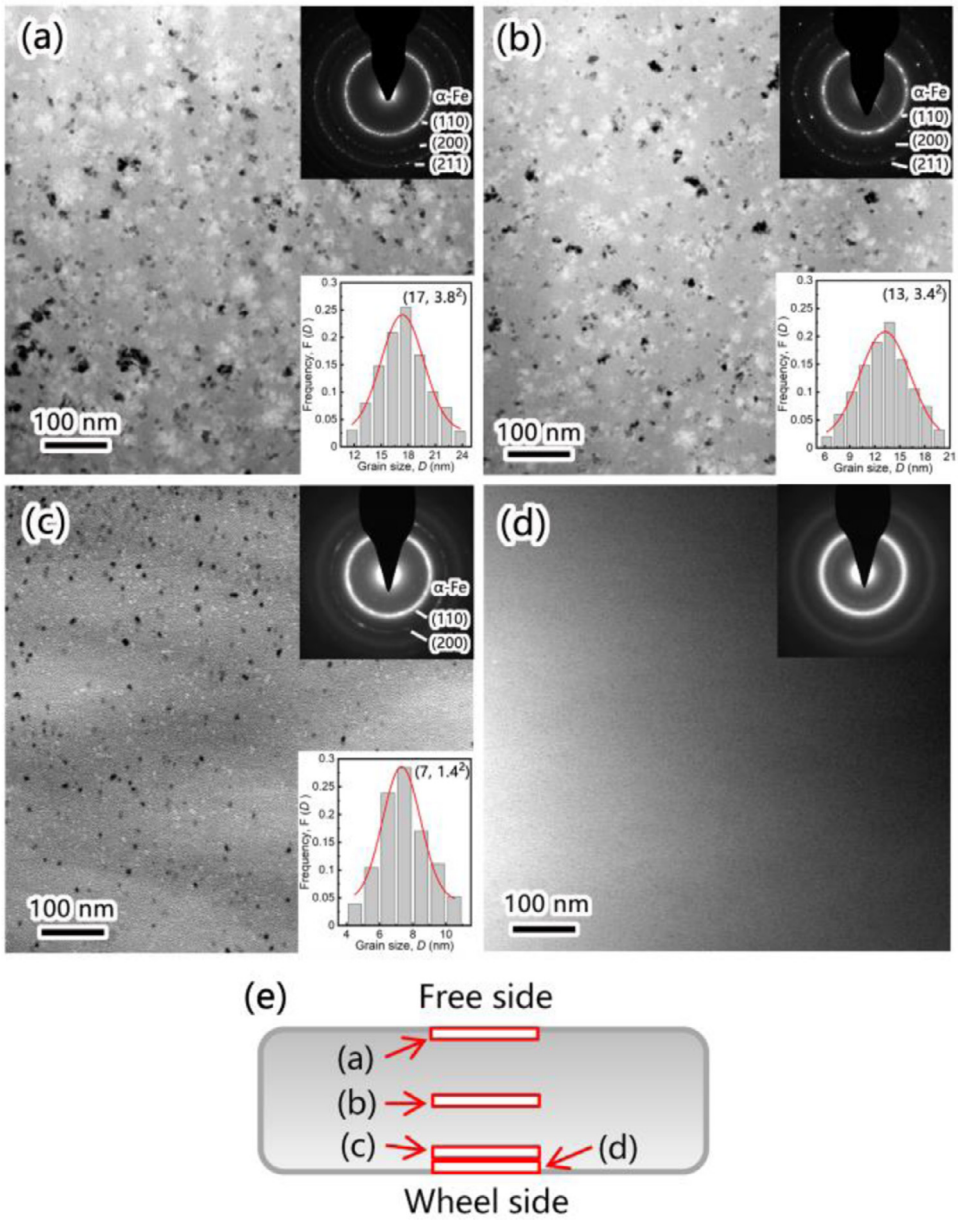

Fig. 3. Bright-field TEM images, corresponding SAED patterns and gain size distributions of different parts (a-d) and their location illustration (e) for as-spun $Fe_{81.3}Si_4B_7C_6Cu_{1.7}$ alloy. (a) Free side surface; (b) central part; (c) shallow surface in wheel side; (d) wheel side surface.

and subsequent nucleation and growth of newly-formed α-Fe crystals during heating, respectively [38]. The T_{x2} changes slightly with the rise of Cu content, indicating that Cu has no obvious effect on formations of non-soft magnetic Fe-B phases.

Fig. 2(a) and (b) shows XRD patterns of free side and DSC curves for as-spun $Fe_{81.3}Si_4B_{13-y}C_yCu_{1.7}$ (y = 0–8) alloys, respectively. For the y = 0–4 alloys, their XRD patterns contain of only broad peaks, but DSC curves have two overlapped exothermic peaks associated with the precipitations of α-Fe phase, suggesting these as-spun alloys possess a composite structure of α-Fe crystals dispersing in amorphous phase [38]. For the y = 6–8 alloys, sharp Bragg peaks that corresponding to α-Fe phase can be found in XRD patterns and the latent heat for precipitation of α-Fe phase in DSC curves is significantly lowered, demonstrating that the rise of C content promotes the formation of α-Fe phase, and thus the rise of C content from 0 to 8 at.% deceases the T_{x1} from 634 to 606 K correspondingly. In addition, a weak Bragg peak belonging to Fe-B phases exists in XRD pattern of the y = 8 alloy and the T_{x2} in its DSC curves are shifted to lower temperature, revealing that the excess C results in the formation of non-soft magnetic phases.

Fig. 3 exhibits the bright-field TEM images, corresponding SAED patterns and gain size distributions of different parts for as-spun y = 6 alloy. It's seen that the y = 6 alloy contains α-Fe crystals with high N_d of about 2×10^{23} m^{-3} in the central part and free side surface. The D and V_{cry} of α-Fe crystals in the central part are estimated as about 13 nm and 40%, respectively, and those in the free side surface are determined as about 17 nm and 50%, respectively. Due to the higher cooling rate, the shallow surface (about 1 μm to the surface) in wheel side of the ribbon has smaller α-Fe crystals, whose N_d and V_{cry} is about 2×10^{23} m^{-3} and 5%, respectively, and the surface is fully amorphous state. Based on the above results, the D and V_{cry} of α-Fe phase in the y = 6 alloy is determined as 12 nm and 32% by arbitrary averaging the values in different parts. In general, the as-spun y = 6 alloy has a combined structure of a full amorphous layer and predominating nanocrystalline structure with gradually increaseing D and V_{cry} of α-Fe crys-

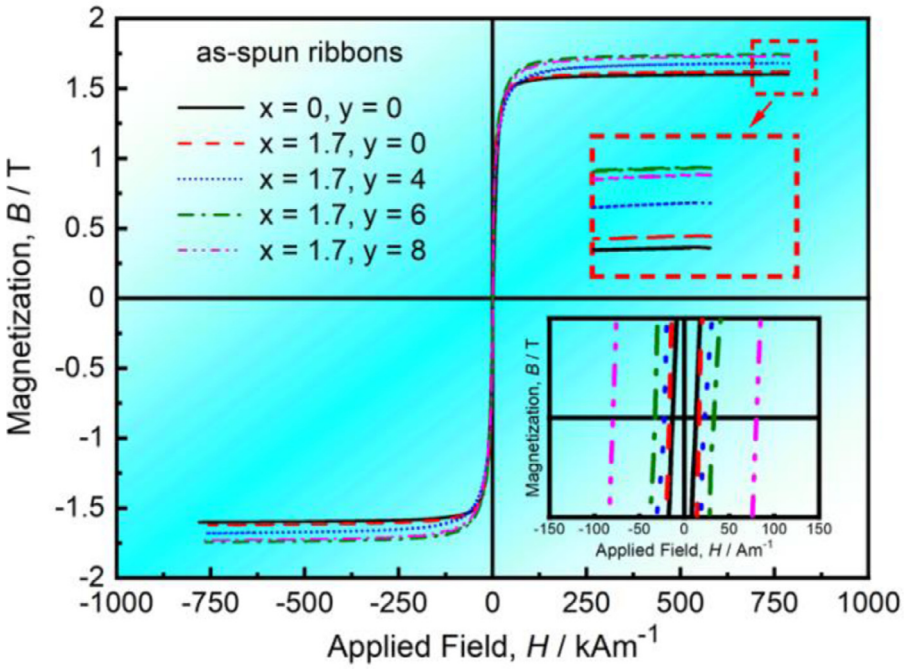

Fig. 4. Hysteresis loops of as-spun $Fe_{83-x}Si_4B_{13-y}C_yCu_x$ alloys. The insets show the enlargements of the loops nears 0 and 800 kA/m.

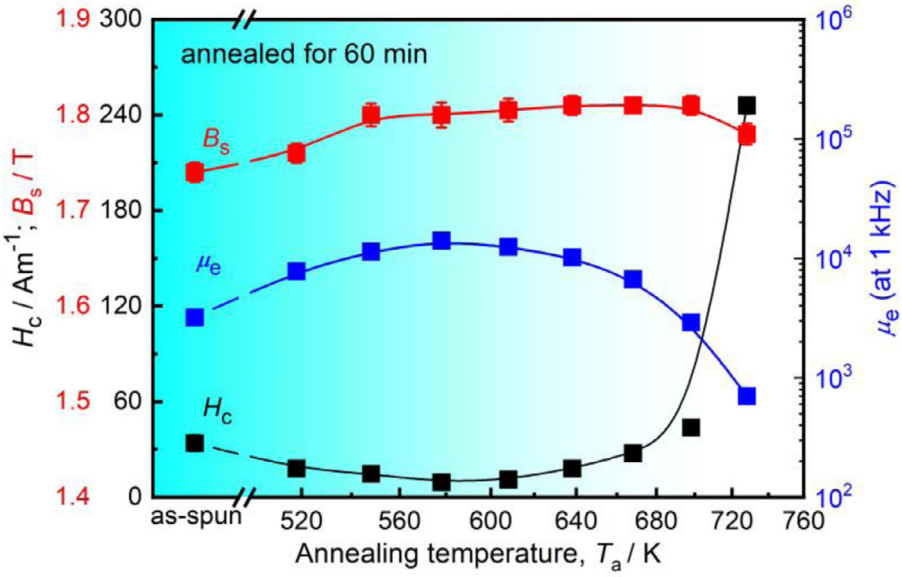

Fig. 5. Variations in B_s, H_c and μ_e as a function of T_a for $Fe_{81.3}Si_4B_7C_6Cu_{1.7}$ alloy.

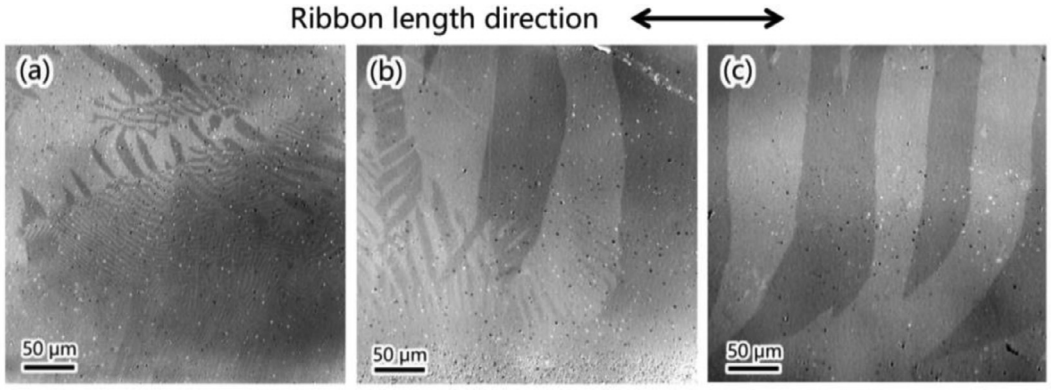

Fig. 6. Magnetic domain structure of $Fe_{81.3}Si_4B_7C_6Cu_{1.7}$ alloy in as-spun state and annealed at various temperatures. (a) As-spun; (b) 518 K; (c) 578 K.

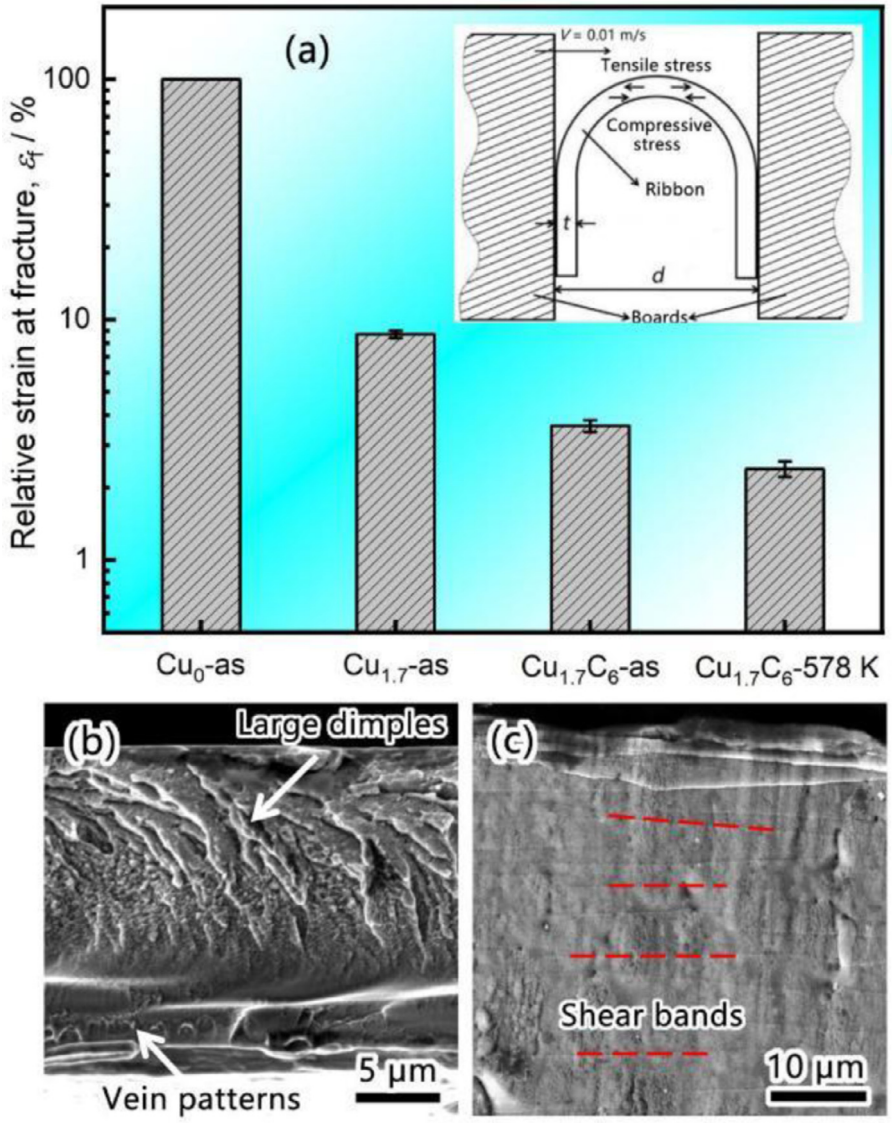

Fig. 7. The ε_f of $Fe_{83-x}Si_4B_{13-y}C_yCu_x$ alloys (a), SEM pictures of fracture surface (b) and wheel side surface (c) for as-spun $Fe_{81.3}Si_4B_7C_6Cu_{1.7}$ nanocrystalline alloy. The inset in (a) shows schematic illustration of the bending tests. The free side of the ribbons in (b) is located at the top of the image.

tals from wheel side to free side. The structure of as-spun $x = 0$–4 alloys is thought to be similar with $x = 6$ alloy. The α-Fe crystals in central part of the $y = 0$ alloy have a similar N_d but much smaller V_{cry} as compared with $y = 6$ alloy, which is agreed with the XRD and DSC results (see Figs. 1(d), 2(a) and (b)), indicating that the rise of C content promotes the precipitation of α-Fe phase.

The above results suggest the rise of C content decreases the AFA of $Fe_{81.3}Si_4B_{13-y}C_yCu_{1.7}$ (y = 0–8) alloys. According to the three-dimensional atom probe results in previous articles [38–41], B and C in Fe-based naocrystalline alloys always distribute in amorphous matrix and are lean in crystal phase due to their limit solubility in α-Fe phase. We noticed that C has a similar atomic size (0.092 nm) but larger negative mixing enthalpy with Fe (−50 kJ/mol) as compared with B (0.098 nm and −26 kJ/mol) [42, 43], hence C should be more powerful than B in promoting amorphous-formation of Fe-based alloys according to empirical rules [44]. However, it's well known that Fe-B binary alloy system could obtain a fully amorphous state by melt-spinning, while Fe-C alloy system can't, which conflicts with the empirical rules. Evteev et al. studied the local atomic ordering of $Fe_{83}M_{17}$ (M = B, C) alloys by a computer simulation method and found that the Fe-B alloy shows a difference in the local compositional orders of crystalline and amorphous states, which raises its AFA, while the Fe-C alloy has identical local compositional order in crystalline and amorphous states and therefore shows a low AFA [45]. According to the composition, the $Fe_{81.3}Si_4B_{13-y}C_yCu_{1.7}$ alloys belong to the Fe-B binary alloy system and a sufficient B content is essential for its AFA, hence the rise of C content decreases their AFA due to the reduction of B content. The $Fe_{81.3}Si_4B_{13-y}C_yCu_{1.7}$ alloys have a high Cu content of 1.7 at.%, and the strong repulsive force between Fe and Cu will result in enrichment of Cu atoms and generate abundant Cu-enriched clusters during melt-spinning, which triggers the nucleation of α-Fe crystals [38]. In addition, some Cu atoms still distribute in amorphous matrix [38]. The high B content of 13 at.% of the $y = 0$ alloy provides it a sufficient AFA, which could significantly suppress the growth of the crystals. The rise of C content lowers the AFA and reduces the suppression effect on the growth of the α-Fe crystals, and then increases the D and V_{cry} of α-Fe phase eventually.

Fig. 4 shows hysteresis loops of as-spun $Fe_{83-x}Si_4B_{13-y}C_yCu_x$ alloys. It's seen that all alloys show typical soft magnetic characteristics. The addition of 1.7 at.% Cu in a $Fe_{83}Si_4B_{13}$ alloy increases B_s

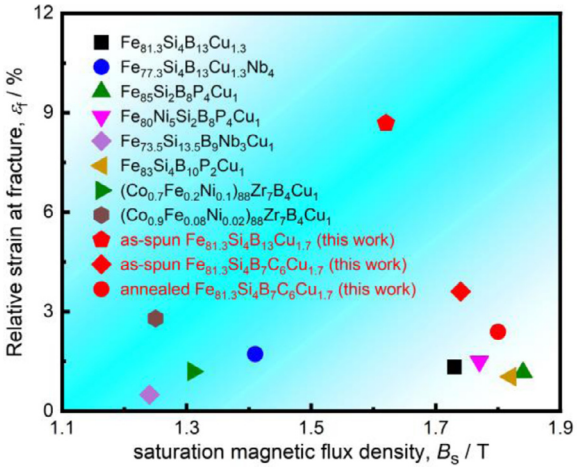

Fig. 8. Comparisons in B_s and ε_f of some nanocrystalline alloys.

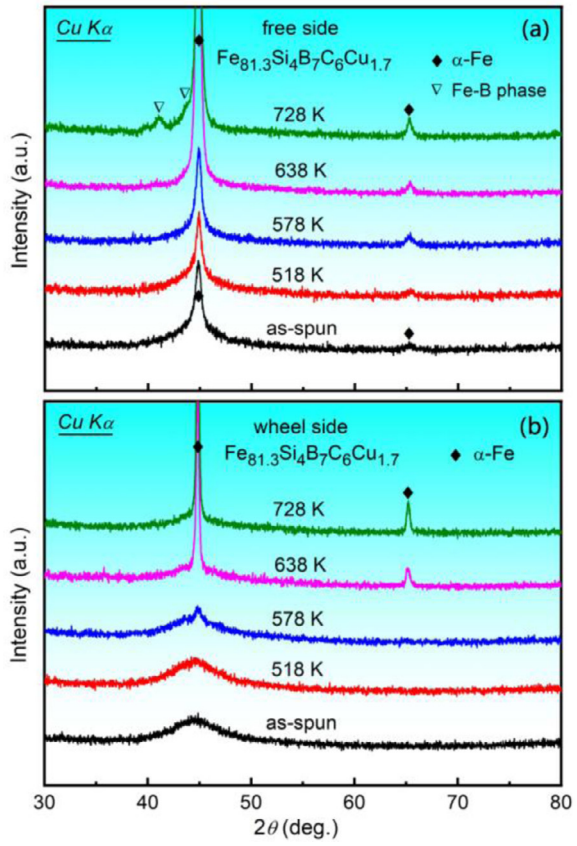

Fig. 9. XRD patterns of free (a) and wheel (b) sides for $Fe_{81.3}Si_4B_7C_6Cu_{1.7}$ alloys in as-spun state and annealed at various temperatures.

and H_c from 1.60 T and 12.7 A/m to 1.62 T and 15.1 A/m, respectively. The rise of C content from 0 to 6 at.% in $Fe_{81.3}Si_4B_{13-y}C_yCu_{1.7}$ alloys increases the B_s and H_c from 1.62 T and 15.1 A/m to 1.74 T and 32.7 A/m, respectively; and the further rise to 8 at.% decreases B_s to 1.73 T and increases H_c to 80.1 A/m. The B_s of Fe-based nanocrystalline alloys is expressed as: $B_s = B_{sc}V_{cry}+B_{sa}(1-V_{cry})$, where B_{sc} and B_{sa} are saturation magnetic flux density of crystal and amorphous phase, respectively. The B_{sc} is over 2.0 T, while the B_{sa} is much smaller [46, 47]. The addition of Cu and rise of C content from 0 to 6 at.% increase the V_{cry}, hence the alloys with higher Cu and C content possess superior B_s. The further increase of C content to 8 at.% results in the formation of Fe-B phase, which may lower the V_{cry}, hence the B_s is reduced.

The magnetic softness of Fe-based amorphous and nanocrystalline alloys are closely related to their average anisotropy constant (K_1) and internal stress, and low H_c can be obtained in the case of small K_1 and internal stress [48]. According to the random anisotropy model, the strong intergranular exchange coupling between the α-Fe crystals could minimize the effect of the magnetocrystalline anisotropy (K) when D is smaller than the exchange-coupled length (L_0, 30–40 nm); hence the alloys with smaller D have lower K_1 [49]. The $x = 0$ alloy has a fully amorphous structure, thus its K_1 should be very low. The addition of Cu and rise of C content from 0 to 6 at.% generate α-Fe crystals and increase the D, thus the K_1 raises gradually; the further rise of C content to 8 at.% leads to the formation of non-soft magnetic Fe-B compounds with much higher K [50], which will significantly increase the K_1. On the other hands, as-spun Fe-based alloys always have strong compressive stress in wheel and free side surfaces of the ribbons [51]. It's well known that crystalline state has a smaller molar volume than corresponding liquid and amorphous states [52]. The rise of Cu and C content in present Fe-Si-B-C–Cu alloys generates a large quantity of α-Fe phases and increases the V_{cry} in the free side; hence the volume reduction of free side during solidification and accordingly compressive stress may be larger than traditional amorphous alloys and increase gradually. As described above, the addition of Cu and rise of C content in present Fe-Si-B-C–Cu alloys increase the K_1 and internal stress, thus the H_c goes up accordingly. We noticed that the magnetic softness of the melt-spun Fe-Si-B-C–Cu alloys is slightly inferior to the typical nanocrystalline alloys, which mainly result from the presence of internal stress in alloy ribbons, because the size of α-Fe crystals in present Fe-Si-B-C–Cu alloys is no larger than that in those alloys.

To further improve the soft magnetic properties, we investigated the effects of annealing on magnetic properties of as-spun $Fe_{81.3}Si_4B_7C_6Cu_{1.7}$ nanocrystalline alloy. Variations in B_s, H_c and μ_e as a function of T_a for the $Fe_{81.3}Si_4B_7C_6Cu_{1.7}$ alloy are exhibited in Fig. 5. Compared with 1.74 T of the as-spun alloy, B_s increases to 1.80 T at 548 K and then remains stable until 698 K, which followed by a slightly decrease to 1.78 T at 728 K. The as-spun alloy shows a H_c of 32.7 A/m and μ_e (at 1 kHz) of 3200, and the rise of T_a to 578 K lowers H_c to 9.4 A/m and increases μ_e to 14,100, which followed slight degradations at 608–698 K and significant deteriorations at 728 K. The magnetic domain structure is mainly depended on the complicated energy balance between magneto static stray field energy, anisotropic magnetic energy and domain wall energy; hence it could reflect the stress status and magnetic properties of the alloys [53–55]. Fig. 6 shows magnetic domain structure of free side surface for $Fe_{81.3}Si_4B_7C_6Cu_{1.7}$ alloys in as-spun state and annealed at various temperatures. The surface of as-spun alloy mainly consists of maze and fine domains. The annealing at 518 K eliminates the maze domains and generates some wide stripe domains, and the rise of T_a to 578 K removes the fine domains and only keeps the wide stripe domains. The maze and fine domains are always associated with internal stress on the surface and the presence of wide stripe domains is beneficial for excellent magnetic softness [56–58]. The domain structure evolution of $Fe_{81.3}Si_4B_7C_6Cu_{1.7}$ alloy demonstrates that the annealing at 518–578 K eliminates the internal stress on the surface and improves their magnetic softness, which agrees with the variations in the H_c and μ_e (see Fig. 5).

Fig. 7(a) exhibits the ε_f of $Fe_{83-x}Si_4B_{13-y}C_yCu_x$ alloys. It's seen that the as-spun $Fe_{83}Si_4B_{13}$ amorphous alloy has a high ε_f of 100%, which means it can be bended to 180° without fracture, demonstrating its excellent ductile. The addition of 1.7 at.% Cu decreases the ε_f of as-spun alloy to 8.69%, illustrates a significantly embrittlement, which can be attributed to the precipitation of α-Fe phase.

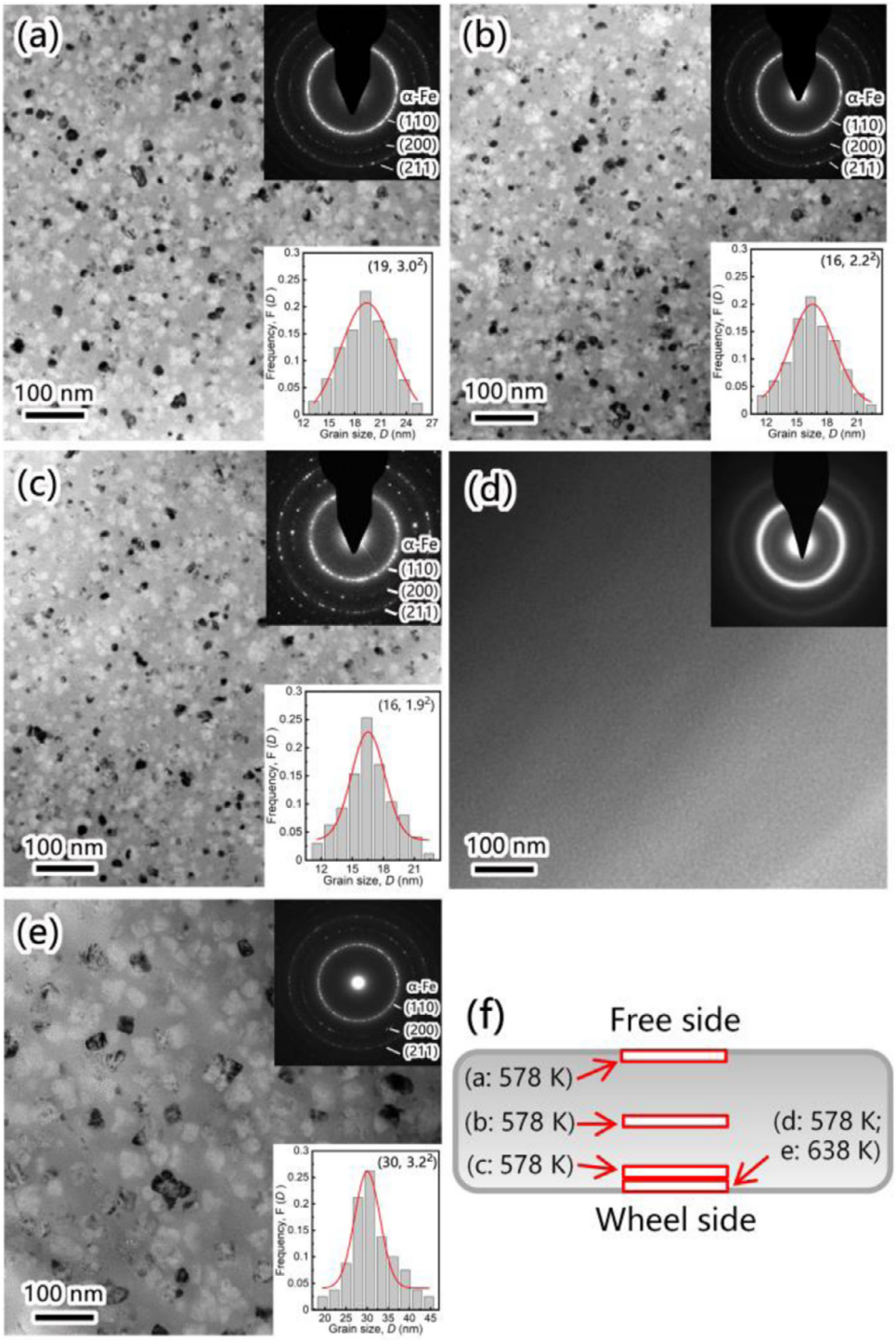

Fig. 10. Bright-field TEM images, corresponding SAED patterns and gain size distributions of different parts (a-e) and their location illustration (f) for annealed $Fe_{81.3}Si_4B_7C_6Cu_{1.7}$ alloys. (a) Free side surface, 578 K; (b) central part, 578 K; (c) shallow surface in wheel side, 578 K; (d) wheel side surface, 578 K; (e) wheel side surface, 638 K.

The α-Fe crystals could act as crack nucleation and result in stress concentration during bending. Consequently, some cracks will form around the α-Fe crystals and propagate rapidly along the interface between the crystals and the amorphous phase, and then the brittle fracture occurred [17, 32]. The addition of 6 at.% C further increases the brittleness of as-spun alloy with decreasing the ε_f to 3.61%, which results from the increases of D and V_{cry} of α-Fe phase. Fig. 7(b) and (c) shows the SEM pictures of fracture surface and wheel side surface for as-spun $Fe_{81.3}Si_4B_7C_6Cu_{1.7}$ nanocrystalline alloy, respectively. The fracture surface contains many large dimples near the free side (see Fig. 7(b)). In addition, the fracture surface near wheel side has some vein patterns (see Fig. 7(b)), and the wheel side surface near the fracture also has many shear bands (see Fig. 7(c)), revealing that plastic deformations occur in the wheel side of the alloy before fracture, which have never been observed on Fe-based nanocrystalline alloys.

Fig. 8 exhibits the comparisons in B_s and ε_f of some nanocrystalline alloys [16, 17, 32, 59-61]. It's seen that the $Fe_{81.3}Si_4B_{13}Cu_{1.7}$

and $Fe_{81.3}Si_4B_7C_6Cu_{1.7}$ nanocrystalline alloys show much higher ε_f than the previous-developed nanocrystalline alloys, declaring a superior ductile of the present Fe-Si-B-C–Cu alloys, which is closely related with their fracture process. The formation of the large dimples needs a much higher energy than smooth fracture surface of previous-developed nanocrystalline alloys [62]; the excellent ductility of the amorphous layer and nanocrystalline structure with small D and low V_{cry} in wheel side could blunt the cracks and decelerate their growth during bending, hence the developed as-spun Fe-Si-B-C–Cu nanocrystalline alloys possess superior ductile. Especially, we noticed that the as-spun $Fe_{81.3}Si_4B_7C_6Cu_{1.7}$ nanocrystalline alloy exhibits a high B_s of 1.74 T and ε_f of 3.61% combined with relatively low H_c of 32.7 A/m and high μ_e (at 1 kHz) of 3200, signifying its superior performances in both soft magnetic properties and ductile. In addition, although the annealing at 578 K slightly decreases ε_f of $Fe_{81.3}Si_4B_7C_6Cu_{1.7}$ alloy to 2.39%, which is still much higher than that of traditional high B_s Fe-based nanocrystalline alloys.

With the aim of understanding the soft magnetic properties and ductile after annealing, we studied the structure of the annealed $Fe_{81.3}Si_4B_7C_6Cu_{1.7}$ alloys. Fig. 9 presents XRD patterns of $Fe_{81.3}Si_4B_7C_6Cu_{1.7}$ alloys in as-spun state and annealed at various temperatures. It's seen that the alloy annealed at 518 K has similar XRD pattern with the as-spun alloy, demonstrating that the annealing has little influence on alloy structure, but only brings about structure relaxation and partial releases the internal stress, thus the B_s and magnetic softness are improved slightly. The rise of T_a to 578 K enhances the intensity of the peaks of free side (see Fig. 9(a)), generates a weak Bragg peak of wheel side in XRD patterns (see Fig. 9(b)), suggesting that the annealing leads to the growth of the pre-existing α-Fe crystals. Fig. 10(a-d) illustrates the TEM pictures, corresponding SAED patterns and gain size distributions of $Fe_{81.3}Si_4B_7C_6Cu_{1.7}$ alloy annealed at 578 K for 60 min. Compared with the as-spun state (see Fig. 3(a-d)), the wheel side surface is still amorphous state and the other parts possess composite structure of α-Fe crystals dispersing in amorphous phase, but the V_{cry} and D of α-Fe phase are increased obviously, which is consistent to the XRD result in Fig. 9. The increase of V_{cry} and further release of internal stress lead to the higher B_s and improved magnetic softness of the alloy annealed at 578 K (see Fig. 5). Meanwhile, the amorphous layer in wheel side surface is remained, thus the ductile of the alloy is still superior to traditional Fe-based nanocrystalline alloys (see Fig. 8). The rise of T_a to 638 K further heightens the Bragg peaks in XRD patterns of free sides and generates a sharp Bragg peak in wheel side (see Fig. 9), which illustrates that the annealing produces some coarse α-Fe crystals in the wheel side of ribbon. The TEM picture and corresponding SAED patterns of wheel side surface for the $Fe_{81.3}Si_4B_7C_6Cu_{1.7}$ alloy annealed at 638 K also prove this (see Fig. 10(e)). Due to the absence of α-Fe crystals in wheel side surface and low H_r of the annealing, the newly-formed α-Fe crystals are relatively coarse (see Fig. 10(e)), which brings about a slightly increase in B_s but worsens the magnetic softness obviously. The annealing at 728 K results in the precipitation of non-soft magnetic Fe-B phase (see Fig. 9(a)), thus it causes the reduction of B_s and remarkable deterioration of magnetic softness (see Fig. 5).

4. Conclusions

In present work, with the aim of synthesizing of Fe-based nanocrystalline alloys with superior soft magnetic properties and ductile by melt-spinning, we investigated the structure, soft magnetic properties and brittleness of melt-spun $Fe_{83-x}Si_4B_{13-y}C_yCu_x$ (x = 0–1.7; y = 0–8) alloys, and studied the effects of annealing on structure and properties evolutions of as-spun $Fe_{81.3}Si_4B_7C_6Cu_{1.7}$ nanocrystalline alloy. The results are summarized as follows:

(1) The addition of 1.7 at.% Cu in a $Fe_{83}Si_4B_{13}$ alloy shifts its as-spun structure from a fully amorphous to a composite of amorphous matrix containing abundant α-Fe crystals with D and V_{cry} of about 6 nm and 5.1%, respectively, and increases B_s and H_c of the alloy from 1.60 T and 12.7 A/m to 1.62 T and 15.1 A/m, respectively.

(2) The rise of C content in $Fe_{81.3}Si_4B_{13-y}C_yCu_{1.7}$ (y = 0–6) alloys promotes the growth of the α-Fe crystals with increasing their D, V_{cry} and B_s, although slightly worsens their magnetic softness. The further rise of C content to 8 at.% results in the precipitation of non-soft magnetic Fe-B phases and deteriorates its soft magnetic properties.

(3) The as-spun $Fe_{81.3}Si_4B_7C_6Cu_{1.7}$ nanocrystalline alloy has a fully amorphous layer in wheel side surface and gradually increasing α-Fe crystal size from wheel to free side, and its D and V_{cry} are determined as about 12 nm and 32%, respectively. The unique structure endows the alloy superior soft magnetic properties and ductile with a high B_s of 1.74 T, H_c of 32.7 A/m, μ_e (at 1 kHz) of 3200 and a high ε_f of 3.61%.

(4) The annealing at 578 K releases internal stress, promotes growth of the α-Fe crystals and remains the amorphous layer of the $Fe_{81.3}Si_4B_7C_6Cu_{1.7}$ alloy, hence improves its magnetic properties and maintains the superior ductile with increasing the B_s and μ_e to 1.80 T and 14,100, respectively, lowering the H_c to 9.4 A/m and slightly reducing ε_f to 2.39%. The annealing at 638–728 K deteriorates the soft magnetic properties by generating coarse α-Fe crystals or non-soft magnetic Fe-B phases.

Declaration of Competing Interest

The authors declare that they have no conflict of interest.

Acknowledgements

This work was financially supported by the National Key Research and Development Program of China (No. 2016YFB0300500), the Youth Innovation Promotion Association CAS (No. 2021294), the National Natural Science Foundation of China (No. 52171153), Ningbo Major Special Projects of the Plan "Science and Technology Innovation 2025" (No. 2018B10084).

References

[1] G. Herzer, Acta Mater 61 (2013) 718–734.
[2] A. Makino, H. Men, T. Kubota, K. Yubuta, A. Inoue, Mater. Trans. JIM 50 (2009) 204–209.
[3] K. Suzuki, N. Kataoka, A. Inoue, A. Makino, T. Masumoto, Mater. Trans. JIM 31 (1990) 743–746.
[4] M.A. Willard, D.E. Laughlin, M.E. McHenry, D. Thoma, K. Sickafus, J.O. Cross, V.G. Harris, J. Appl. Phys. 84 (1998) 6773–6777.
[5] M. Ohta, Y. Yoshizawa, J. Appl. Phys. 103 (2008) 07E722.
[6] A. Makino, T. Kubota, K. Yubuta, A. Inoue, A. Urata, H. Matsumoto, S. Yoshida, J. Appl. Phys. 109 (2011) 07A302.
[7] Y. Yoshizawa, S. Oguma, K. Yamauchi, J. Appl. Phys. 64 (1988) 6044–6046.
[8] Y. Zhang, P. Sharma, A. Makino, IEEE Trans. Magn. 50 (2014) 2003004.
[9] A. Makino, IEEE Trans. Magn. 48 (2012) 1331–1335.
[10] K. Suzuki, R. Parsons, B.W. Zang, K. Onodera, H. Kishimoto, A. Kato, Appl. Phys. Lett. 110 (2017) 012407.
[11] B.W. Zang, R. Parsons, K. Onodera, H. Kishimoto, A. Kato, A.C.Y. Liu, K. Suzuki, Scr. Mater. 132 (2017) 68–72.
[12] X.D. Fan, T. Zhang, M.F. Jiang, W.M. Yang, B.L. Shen, J. Non-Cryst. Solids 503–504 (2019) 36–43.
[13] M.E. McHenry, M.A. Willard, D.E. Laughlin, Prog. Mater. Sci. 44 (1999) 291–433.
[14] Y. Yoshizawa, Scr. Mater. 44 (2001) 1321–1325.
[15] P. Sharma, X. Zhang, Y. Zhang, A. Makino, Scr. Mater. 95 (2015) 3–6.
[16] Y. Meng, S.J. Pang, C.T. Chang, X.Y. Bai, T. Zhang, J. Magn. Magn. Mater. 523 (2021) 167583.
[17] Y.H. Li, G.Z. Zhang, L.C. Wu, W. Zhang, J. Mater. Sci. 56 (2021) 2572–2583.
[18] L. Xie, A.D. Wang, S.Q. Yue, A.N. He, C.T. Chang, Q. Li, X.M. Wang, C.T. Liu, J. Magn. Magn. Mater. 483 (2019) 158–163.
[19] J.H. Zhang, F.P. Wan, Y.C. Li, J.C. Zheng, A.D. Wang, J.C. Song, M.Q. Tian, A.N. He, C.T. Chang, J. Magn. Magn. Mater. 438 (2017) 162–131.
[20] E. Lopatina, I. Soldatov, V. Budinsky, M. Marsilius, L. Schultz, G. Herzer, R. Schäfer, Acta Mater 96 (2015) 10–17.

[21] T. Liu, A.N. He, F.Y. Kong, A.D. Wang, Y.Q. Dong, X.M. Wang, H. Zhang, H.W. Ni, Y. Yang, J. Mater. Sci. Technol. 68 (2021) 53–60.
[22] J.G. Wang, H. Zhao, C.X. Xie, C.T. Chang, S.M. Zhou, J.Q. Feng, J.T. Huo, W.H. Li, J. Alloys Compd. 790 (2019) 524–528.
[23] K. Hono, D.H. Ping, M. Ohnuma, H. Onodera, Acta Mater 47 (1999) 997–1006.
[24] M. Matsuura, M. Nishijing, K. Takenaka, A. Takeuchi, H. Ofuchi, A. Makino, J. Appl. Phys. 117 (2015) 17A324.
[25] M. Ohta, Y. Yoshizawa, Jpn. J. Appl. Phys. 46 (2007) L477–L479.
[26] L.X. Shi, K.F. Yao, Mater. Des. 189 (2020) 108511.
[27] L. Shi, X. Qin, K. Yao, Prog. Nat. Sci. Mater. 30 (2020) 208–212.
[28] Y.Q. Xu, Y.H. Li, Z.W. Zhu, W. Zhang, J. Non-Cryst. Solids 487 (2018) 60–64.
[29] Y.H. Li, W. Zhang, T.L. Qi, J. Alloys Compd. 693 (2017) 25–31.
[30] Y. Wu, X.D. Hui, Z.P. Lu, Z.Y. Liu, L. Liang, G.L. Chen, J. Alloys Compd. 467 (2009) 187–190.
[31] W. Li, Y.H. Yang, C.X. Xie, Y.Z. Yang, H.Y. Liu, K.W. Wang, Z.L. Liao, J. Magn. Magn. Mater. 498 (2020) 166128.
[32] X.J. Jia, Y.H. Li, L.C. Wu, W. Zhang, J. Alloys Compd. 822 (2020) 152784.
[33] X.J. Jia, Y.H. Li, L.C. Wu, Y. Zhang, L. Xie, W. Zhang, J. Mater. Sci. 54 (2019) 4400–4408.
[34] Y.H. Li, X.J. Jia, Y.Q. Xu, C.T. Chang, G.Q. Xie, W. Zhang, J. Alloys Compd. 722 (2017) 859–863.
[35] C. Wu, H.P. Chen, H.P. Lv, M. Ya, J. Alloys Compd. 673 (2016) 278–282.
[36] P. Allia, J. Appl. Phys. 74 (1993) 3137–3143.
[37] W.L. Liu, Y.G. Wang, F.G. Chen, J. Mater. Sci.-Mater. Electron. 25 (2014) 5066–5070.
[38] Y.H. Li, X.J. Jia, W. Zhang, Y. Zhang, G.Q. Xie, Z.Y. Qiu, J.H. Luan, Z.B. Jiao, J. Mater. Sci. Technol. 65 (2021) 171–181.
[39] Y.M. Chen, T. Ohkubob, M. Ohta, Y. Yoshizawa, K. Hono, Acta Mater 57 (2009) 4463–4472.
[40] S. Jafari, A. Beitollahi, B. E.Yekta, T. Ohkubo, V. Budinsky, M. Marsilius, G. Herzer, K. Hono, J. Alloys Compd. 674 (2016) 136–144.
[41] Y. Wu, H.X. Li, J.E. Gao, H. Wang, X.J. Liu, M.K. Miller, H. Bei, Y.F. Gao, Z.P. Lu, J. Alloys Compd. 688 (2016) 822–827.
[42] A. Takeuchi, A. Inoue, Mater. Trans. JIM 46 (2005) 2817–2829.
[43] O.N. Senkov, D.B. Miracle, Mater. Res. Bull. 36 (2001) 2183–2198.
[44] A. Inoue, Acta Mater 48 (2000) 279–306.
[45] A.V. Evteev, A.T. Kosilov, E.V. Levtchenko, Acta Mater 51 (2003) 2665–2674.
[46] M. Ohta, Y. Yoshizawa, J. Magn. Magn. Mater. 321 (2009) 2220–2224.
[47] L. Hou, X.D. Fan, W.M.Yang Q.Q.Wang, B.L. Shen, J. Mater. Sci. Technol. 35 (2019) 1655–1661.
[48] W. Zhang, X.J. Jia, Y.H. Li, C.F. Fang, J. Appl. Phys. 115 (2014) 17A768.
[49] G. Herzer, IEEE Trans. Magn. 26 (1990) 1397–1402.
[50] G. Herzer, J. Magn. Magn. Mater. 294 (2005) 99–106.
[51] M. Tejedor, J.A. GarcmHa, J. Carrizo, L. Elbaile, J.D. Santos, J. Magn. Magn. Mater. 202 (1999) 485–491.
[52] F.E. Luborsky, J.L. Walter, J. Appl. Phys. 47 (1976) 1276–1281.
[53] R. Sahingoz, M. Erol, M.R.J. Gibbs, J. Magn. Magn. Mater. 271 (2004) 74–78.
[54] P.B. Chen, A.D. Wang, C.L. Zhao, A.N. He, G. Wang, C.T. Chang, X.M. Wang, C.T. Liu, Sci. China Phys. Mech. 60 (2017) 1–6.
[55] P.B. Chen, T. Liu, F.Y. Kong, A.D. Wang, C.Y. Yu, C.T.Chang G.Wang, X.M. Wang, J. Mater. Sci. Technol. 34 (2018) 793–798.
[56] F.L. Schafer, A. Hubert, G. Herzer, J. Appl. Phys. 69 (1991) 5325.
[57] H. Kronmüller, M. Fähnle, M. Domann, H. Grimm, R. Grimm, B. Gröger, J. Magn. Magn. Mater. 13 (1979) 53–70.
[58] X.H. Zhang, Y.Q. Dong, A.N. He, L. Xie, F.S. Li, L. Chang, H.Y. Xiao, H. Li, T. Wang, J. Magn. Magn. Mater. 506 (2020) 166757.
[59] T.M. Heil, K.J. Wahl, A.C. Lewis, J.D. Mattison, M.A. Willard, Appl. Phys. Lett. 90 (2007) 212508.
[60] T.M. Heil, M.A. Willard, J.J. Flores, J. Appl. Phys. 101 (2007) 09N107.
[61] I. Skorvanek, R. Gerling, J. Appl. Phys. 72 (1992) 3417.
[62] M. Daniil, P.R. Ohodnicki, M.E. McHenry, M.A. Willard, Philos. Mag. 90 (2010) 1547–1565.